Figures and figure supplements

Inter- and intra-animal variation in the integrative properties of stellate cells in the medial entorhinal cortex

Hugh Pastoll *et al*

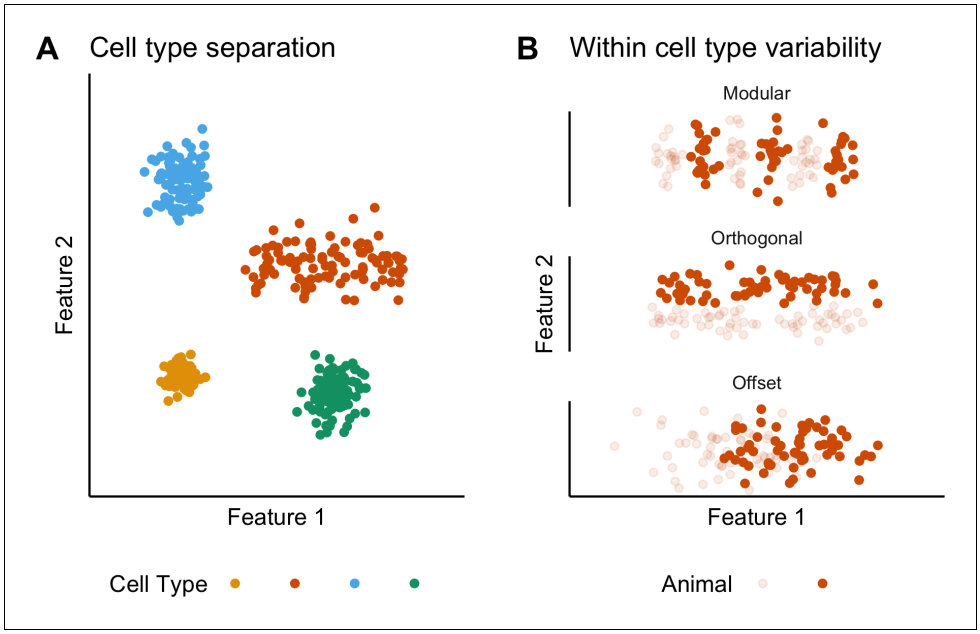

Figure 1. Classification and variability of neuronal cell types. (**A**) Neuronal cell types are identifiable by features clustering around a distinct point (blue, green and yellow) or a line (orange) in feature space. The clustering implies that neuron types are defined by either a single set point (blue, green and yellow) or by multiple set points spread along a line (orange). (**B**) Phenotypic variability of a single neuron type could result from distinct set points that subdivide the neuron type but appear continuous when data from multiple animals are combined (modular), from differences in components of a set point that do not extend along a continuum but that in different animals cluster at different locations in feature space (orthogonal), or from differences between animals in the range covered by a continuum of set points (offset). These distinct forms of variability can only be made apparent by measuring the features of many neurons from multiple animals.

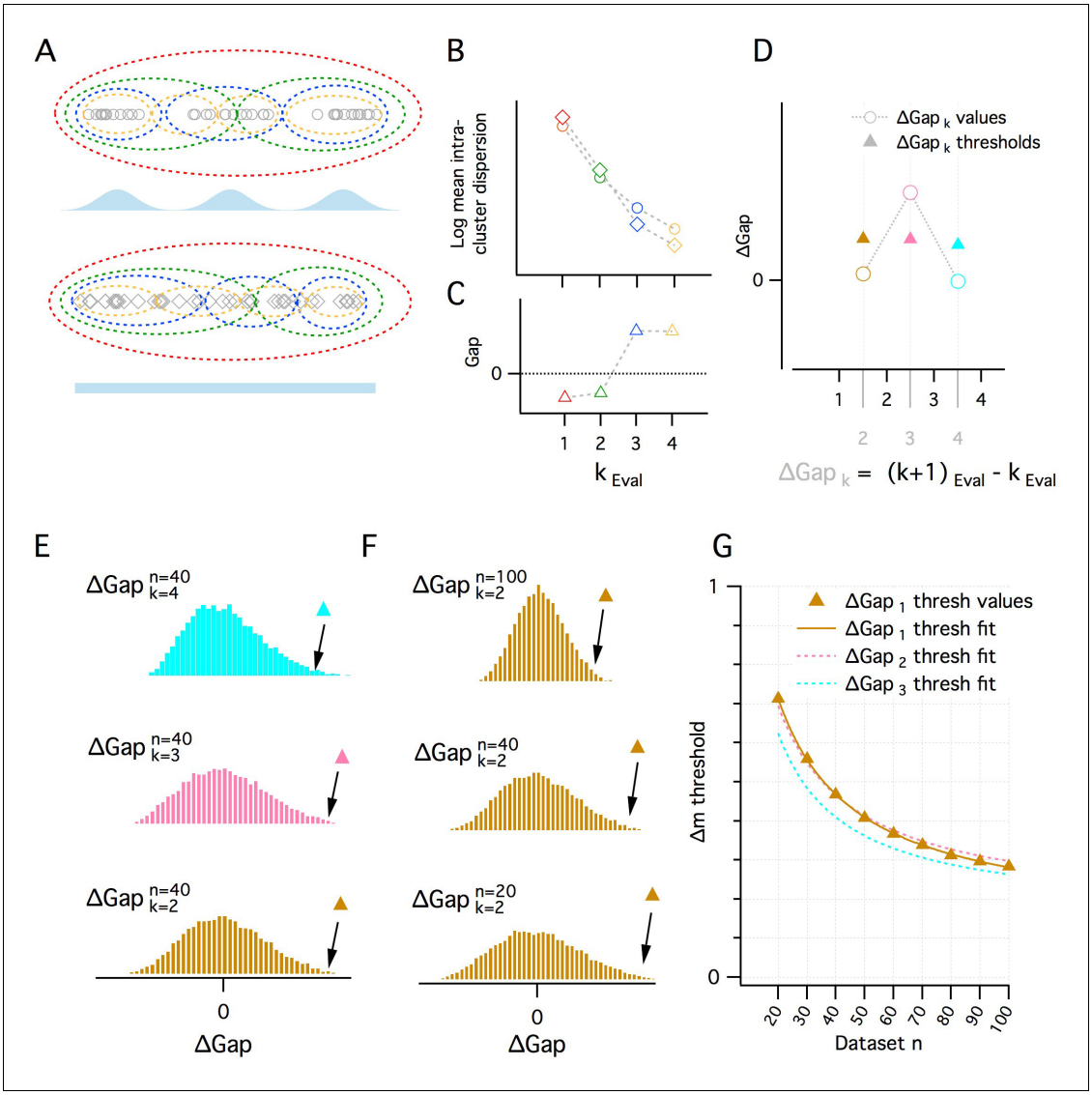

Figure 1—figure supplement 1. A quantitative adaptation of the gap statistic clustering algorithm. (**A–C**) Logic of the gap statistic. (**A**) Simulated clustered dataset with three modes (k = 3) (open gray circles) (upper) and the corresponding simulated reference dataset drawn from a uniform distribution with lower and upper limits set by the minimum and maximum values from the corresponding clustered dataset (open gray diamonds). Data were allocated to clusters by running a K-means algorithm 20 times on each set of data and selecting the partition with the lowest average intracluster dispersion. Red, green, blue and yellow dashed ovals show a realization of the data subsets allocated to each cluster when k_{Eval} = 1, 2, 3 and 4 modes. (**B**) The average value of the log intracluster dispersion for the clustered (open circles) and reference (open diamonds) datasets for each value of k tested in panel (**A**). (**C**) Gap values resulting from the difference between the clustered and reference values for each k in panel (**B**). Many (≥500 in this paper) reference distributions are generated and their mean intracluster dispersion values are subtracted from those arising from the clustered distribution to maximize the reliability of the Gap values. (**D**) A procedure for selecting the optimal k depending on the associated gap values. Quantitative procedure for selecting optimal k (k_{est}). ΔGap values (open circles) are obtained by subtracting from the Gap value of a given k the Gap value for the previous k ($\Delta Gap_k = Gap_k - Gap_{k-1}$). For each ΔGap_k, if the ΔGap value is greater than a threshold (filled triangles) associated with that ΔGap_k, that ΔGap_k will be k_{est}, if no ΔGap exceeds, the threshold, k_{est} = 1. In the figure, for ΔGap_k = 2, 3, 4 (brown, pink and cyan), the ΔGap value exceeds its threshold only when ΔGap_k = 3. Therefore k_{est} = 3. (**E–G**) Determination of ΔGap_k thresholds. (**E**) Histograms of ΔGap values calculated from 20,000 simulated datasets drawn from uniform distributions for each ΔGap_k (brown, pink and cyan, respectively, for ΔGap_k = 2, 3, 4) for a single dataset size (n = 40). ΔGap thresholds (filled triangles) are the values beyond which 1% of the ΔGap values fall and vary with ΔGap_k. (**F**) Histograms of ΔGap values for a range of dataset sizes (n = 20, 40, 100) and their associated thresholds. (**G**) Plot of the ΔGap thresholds as a function of dataset size and ΔGap_k. For separate ΔGap_k, ΔGap threshold values are fitted well by a hyperbolic function of dataset size. These fits provide a practical method of finding the appropriate ΔGap threshold for an arbitrary dataset size.

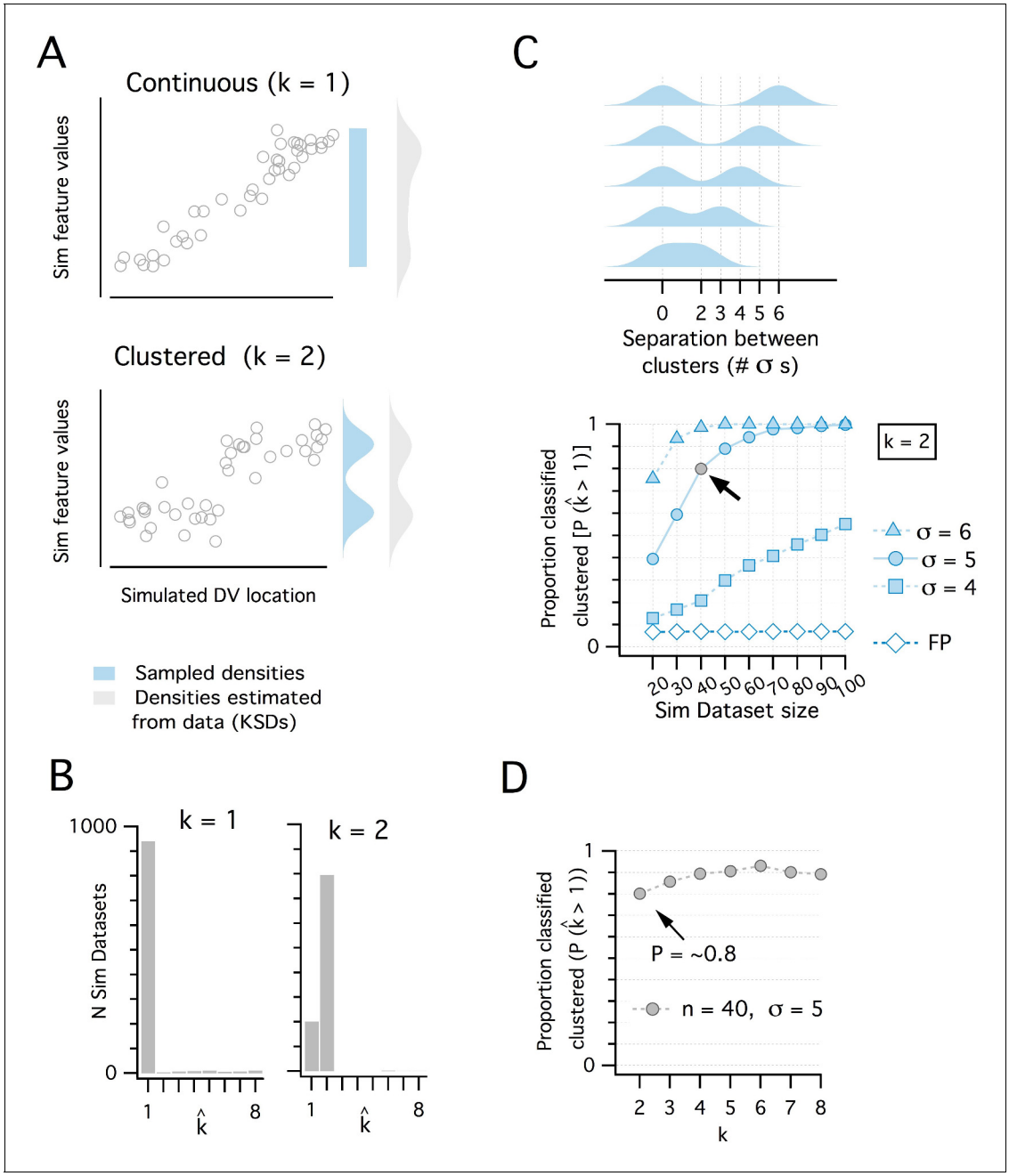

Figure 1—figure supplement 2. Discrimination of continuous from modular organizations using the adapted gap statistic algorithm. (**A**) Simulated datasets (each n = 40) drawn from continuous (uniform, k = 1 mode) (upper) and modular (multimodal mixture of Gaussians with k = 2 modes) (lower) distributions, and plotted against simulated dorsoventral locations. Also shown are the probability density functions (pdf) used to generate each dataset (light blue) and the densities estimated post-hoc from the generated data as kernel smoothed densities (light gray pdfs). (**B**) Histograms showing the distribution of k_{est} from 1000 simulated datasets drawn from each pdf in panel (**A**). k_{est} is determined for each dataset by a modified gap statistic algorithm (see ***Figure 1—figure supplement 1*** above). When k_{est} = 1, the dataset is considered to be continuous (unclustered), when $k_{est} \geq 2$, the dataset is considered to be modular (clustered). The algorithm operates only on the feature values and does not use location information. (**C**) Illustration of a set of clustered (k = 2) pdfs with the distance (in standard deviations) between clusters ranging from 2 to 6 (upper). Systematic evaluation of the ability of the modified gap statistic algorithm to detect clustered organization ($k_{est} \geq 2$) in simulated datasets of different size (n = 20 to 100) drawn from the clustered (filled blue) and continuous (open blue) pdfs (lower). The proportion of datasets drawn from the continuous distribution that have $k_{est} \geq 2$ is the false positive (FP) rate (pFP = ~0.07). The light gray filled circle shows the smallest dataset size (n = 40) with SD = 5, where the proportion of datasets detected as clustered (p_{detect}) is ~0.8. (**D**). Plot showing how p_{detect} at n = 40, SD = 5 changes when datasets are drawn from pdfs with different numbers of clusters (n modes from 2 to 8). Further evaluation of the analysis of additional clusters is represented in the following figure.

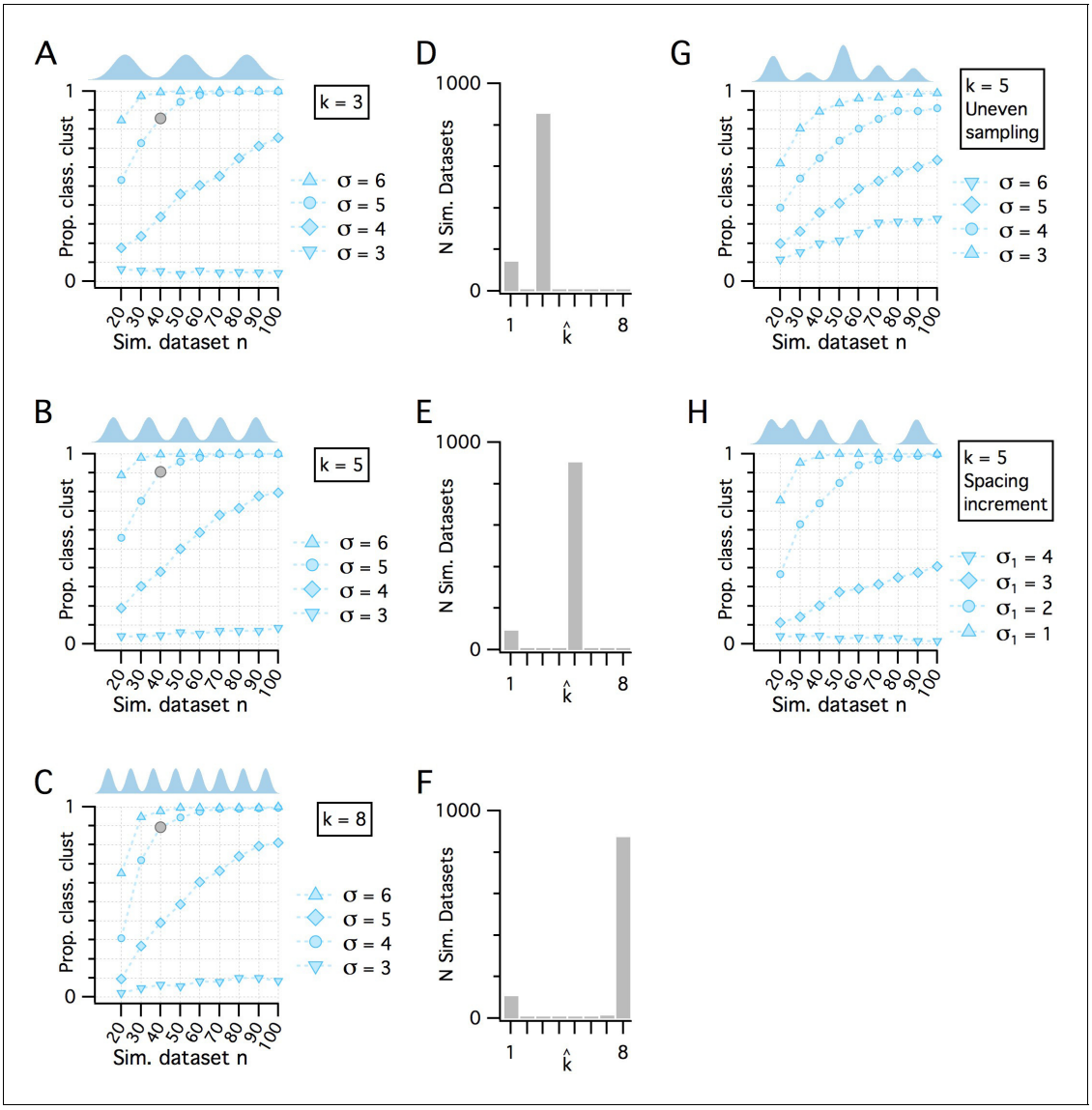

Figure 1—figure supplement 3. Additional evaluation of the adapted gap statistic algorithm. (**A–C**) Plots showing how p_{detect} (the ability of the modified gap statistic algorithm to detect clustered organization) depends on dataset size and separation between cluster modes in simulated datasets drawn from clustered pdfs with different numbers of modes. The gray markers indicate n = 40, SD = 5 (as shown in ***Figure 1E***). In each plot, p_{detect} is shown as a function of simulated dataset size and separation between modes when k = 3 (**A**), k = 5 (**B**) and k = 8 (**C**), which was the maximum number of clusters evaluated. (**D–F**) Histograms showing the counts of k_{est} from the 1000 simulated n = 40, SD = 5 datasets (gray filled circles) illustrated in panels (**A–C**), respectively. (**G**) p_{detect} as a function of dataset size and mode separation with k = 5 when cluster modes are unevenly sampled. Sample sizes from clusters vary randomly with each dataset. A single mode can contribute from all to none of the points in any simulated dataset. (**H**) p_{detect} as a function of dataset size and mode separation with k = 5 when the distance between mode centers increases by a factor of sqrt(2) between sequential cluster pairs. Data are shown for different initial separations (the distance between the first two cluster centers) ranging from 1 to 4 (with corresponding separations between the final cluster pair ranging from 4 to 16).

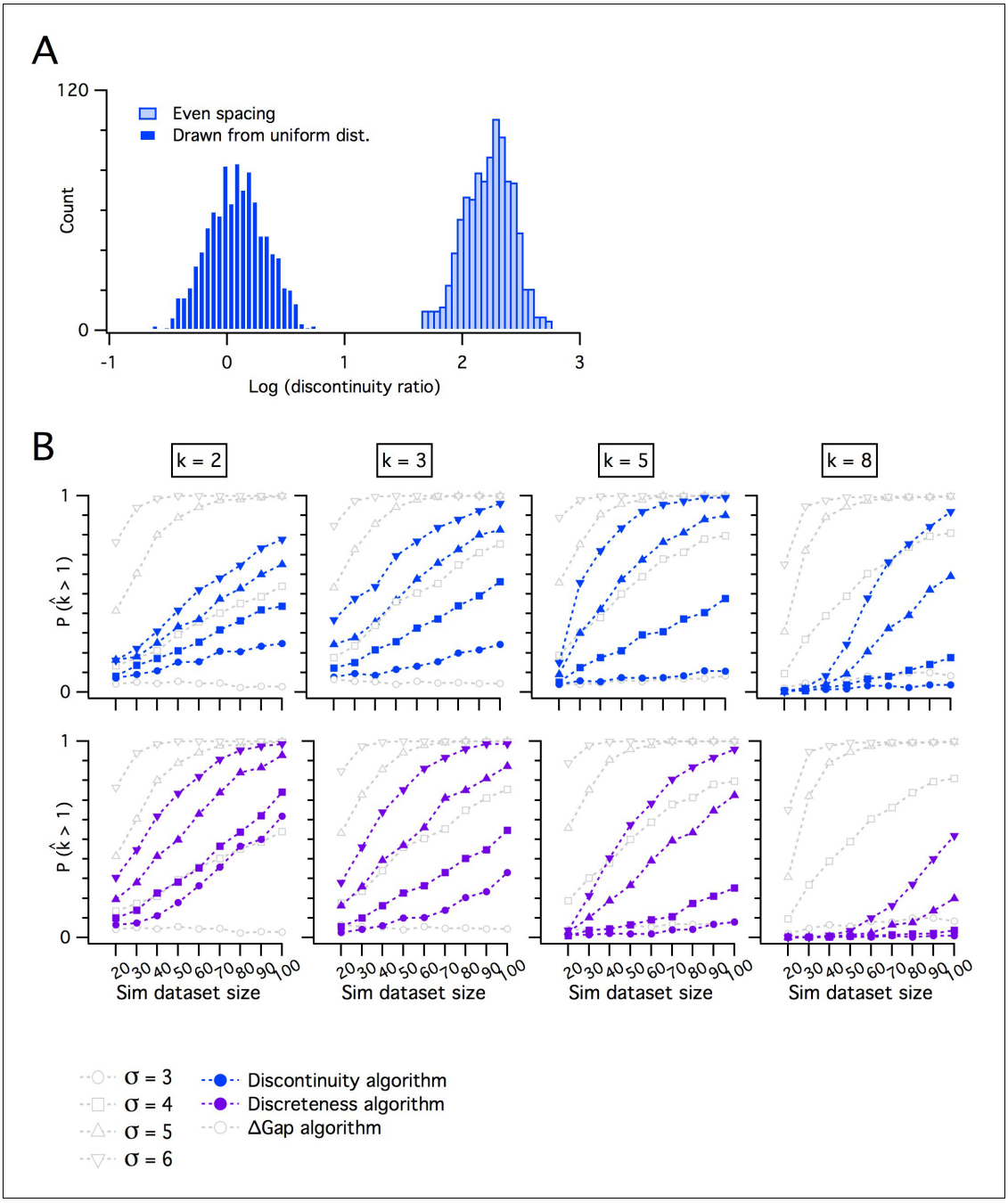

Figure 1—figure supplement 4. Comparing the adapted gap statistic algorithm with discontinuity measures for discreteness. (**A**) Counts of log discontinuity ratio scores generated from a simulated uniform data distribution. The data distribution was ordered and then sampled either at positions drawn at random from a uniform distribution (dark blue) or at positions with a fixed increment (light blue). For the data sampled at random positions, approximately half of the scores are >0 and for even sampling all scores are >0. Therefore, a threshold score >0 does not distinguish discrete from continuous distributions. (**B**) Comparison of p_{detect} as a function of dataset size for the adapted gap statistic algorithm, the discontinuity (upper) and the discreteness algorithm (lower). Each algorithm is adjusted to yield a 7% false positive rate. Each column shows simulations of data with different numbers of modes (k).

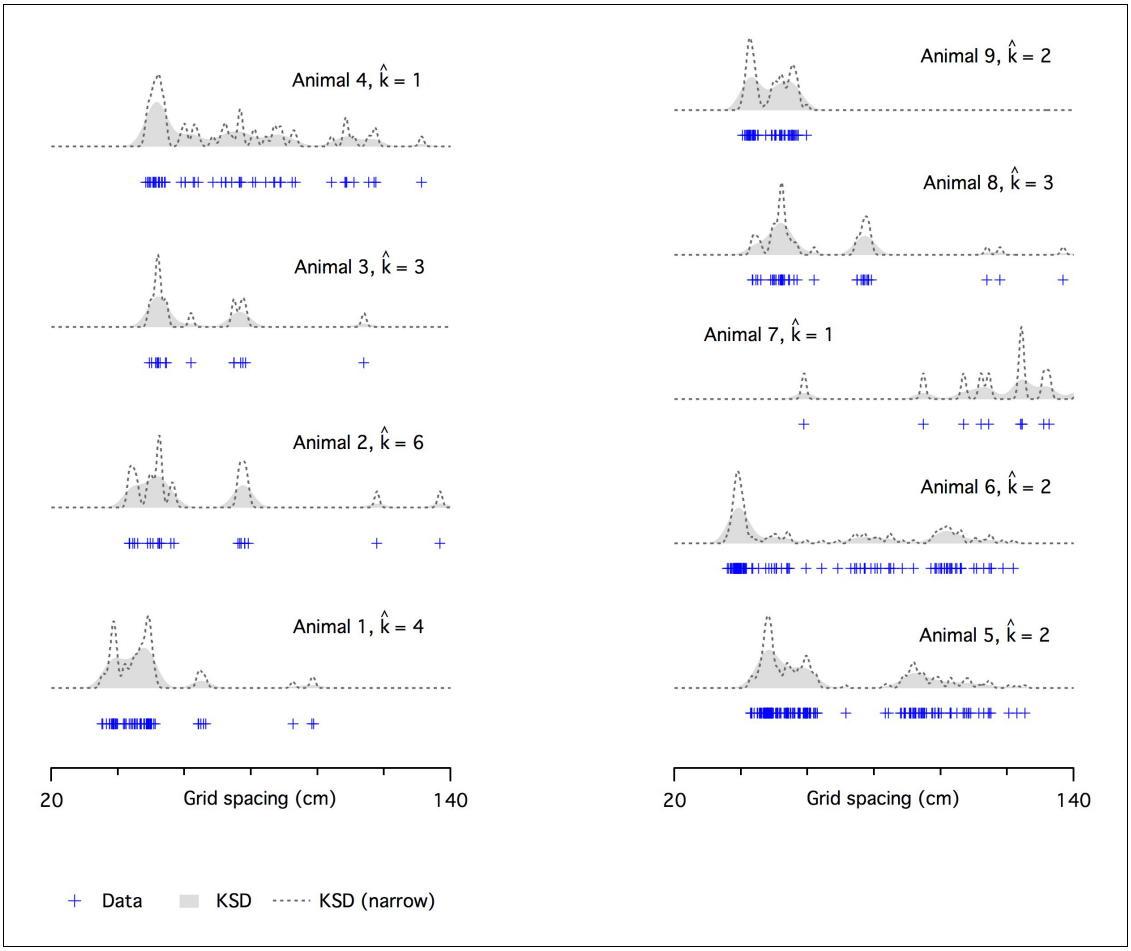

Figure 1—figure supplement 5. Evaluation of modularity of grid firing using an adapted gap statistic algorithm. Examples of grid spacing for individual neurons (crosses) from different mice. Kernel smoothed densities (KSDs) were generated with either a wide (solid gray) or a narrow (dashed lines) kernel. The number of modes estimated using the modified gap statistic algorithm is ≥ 2 for all but one animal (animal 4) with $n \geq 20$ (animals 3 and 7 have < 20 recorded cells). We did not have location information for animal 2.

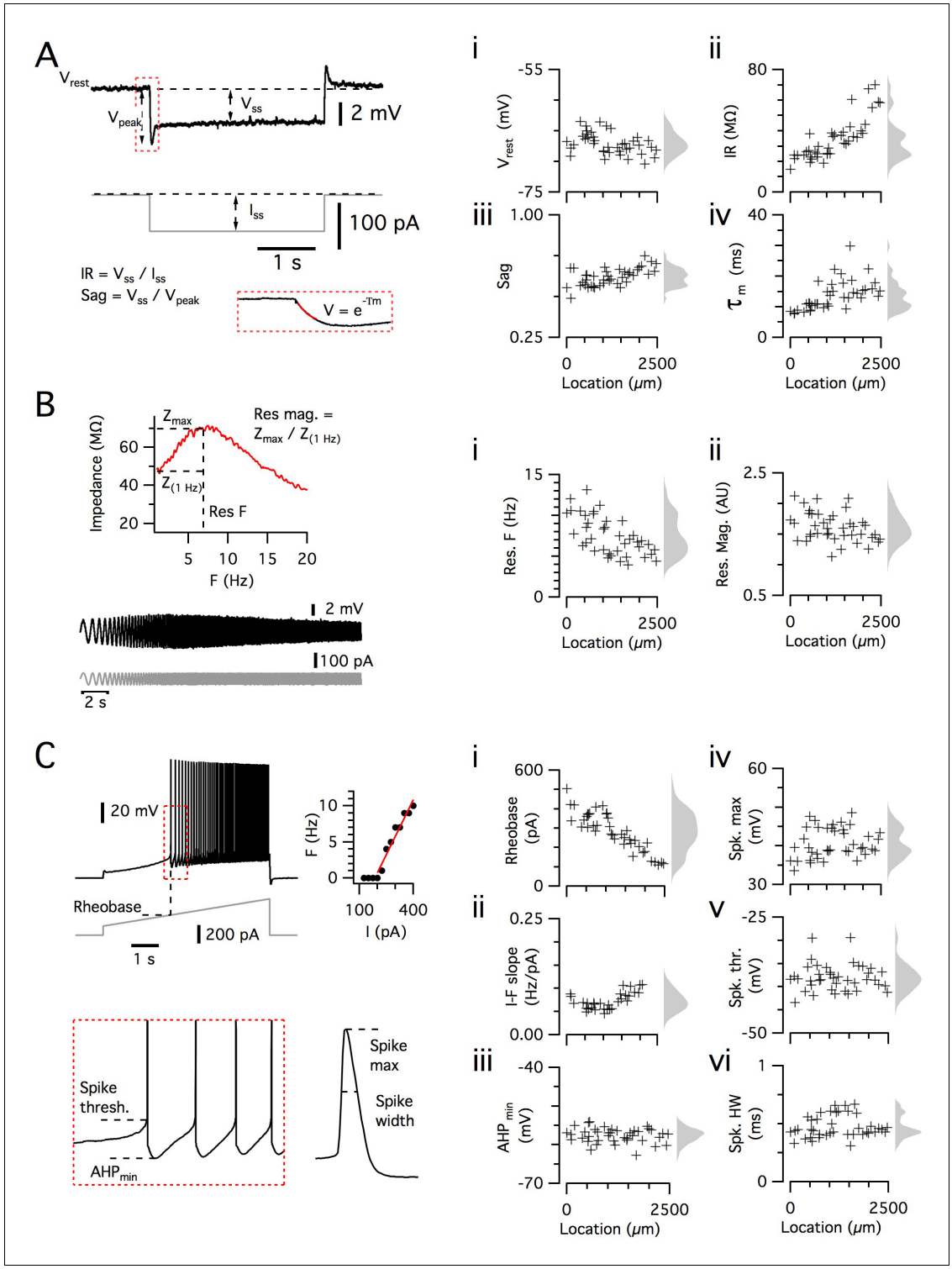

Figure 2. Dorsoventral organization of intrinsic properties of stellate cells from a single animal. (**A–C**) Waveforms (gray traces) and example responses (black traces) from a single mouse for step (**A**), ZAP (**B**) and ramp (**C**) stimuli (left). The properties derived from each protocol are shown plotted against recording location (each data point is a black cross) (right). KSDs with arbitrary bandwidth are displayed to the right of each data plot to facilitate visualization of the property's distribution when location information is disregarded (light gray pdfs). (**A**) Injection of a series of current steps enables the measurement of the resting membrane potential (V_{rest}) (**i**), the input resistance (IR) (ii), the sag coefficient (sag) (iii) and the membrane time constant (τ_m) (iv). (**B**) Injection of ZAP current waveform enables the calculation of an impedance amplitude profile, which was used to estimate the resonance resonant frequency (Res. F) (**i**) and magnitude (Res. mag) (ii). (**C**) Injection of a slow current ramp enabled the measurement of the rheobase (i); the

Figure 2 continued on next page

Figure 2 continued

slope of the current-frequency relationship (I-F slope) (ii); using only the first five spikes in each response (enlarged zoom, lower left), the AHP minimum value (AHP_{min}) (iii); the spike maximum (Spk. max) (iv); the spike threshold (Spk. thr.) (v); and the spike width at half height (Spk. HW) (vi).

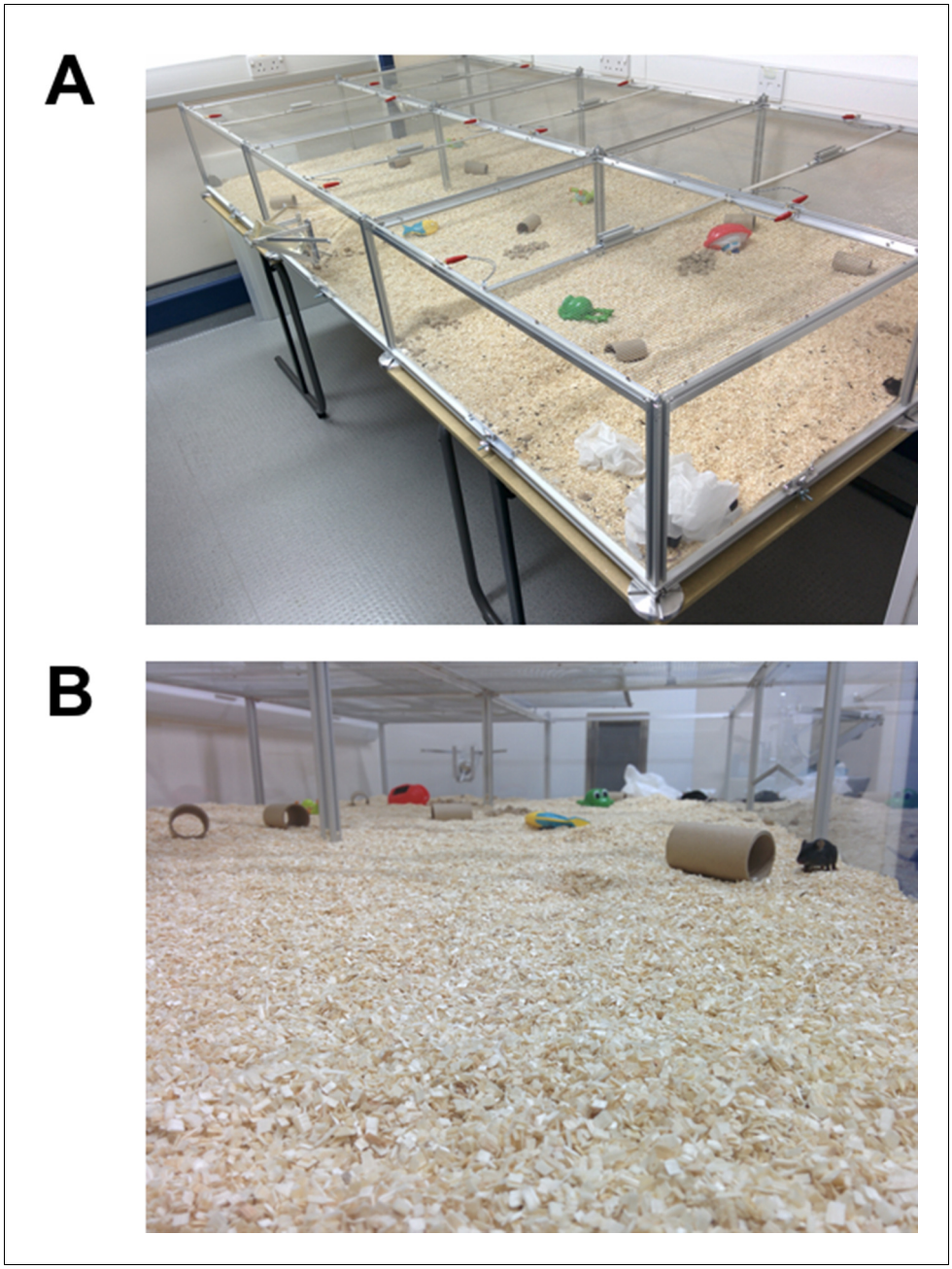

Figure 2—figure supplement 1. Large environment for housing. (**A, B**) The large cage environment viewed from above (**A**) and from inside (**B**).

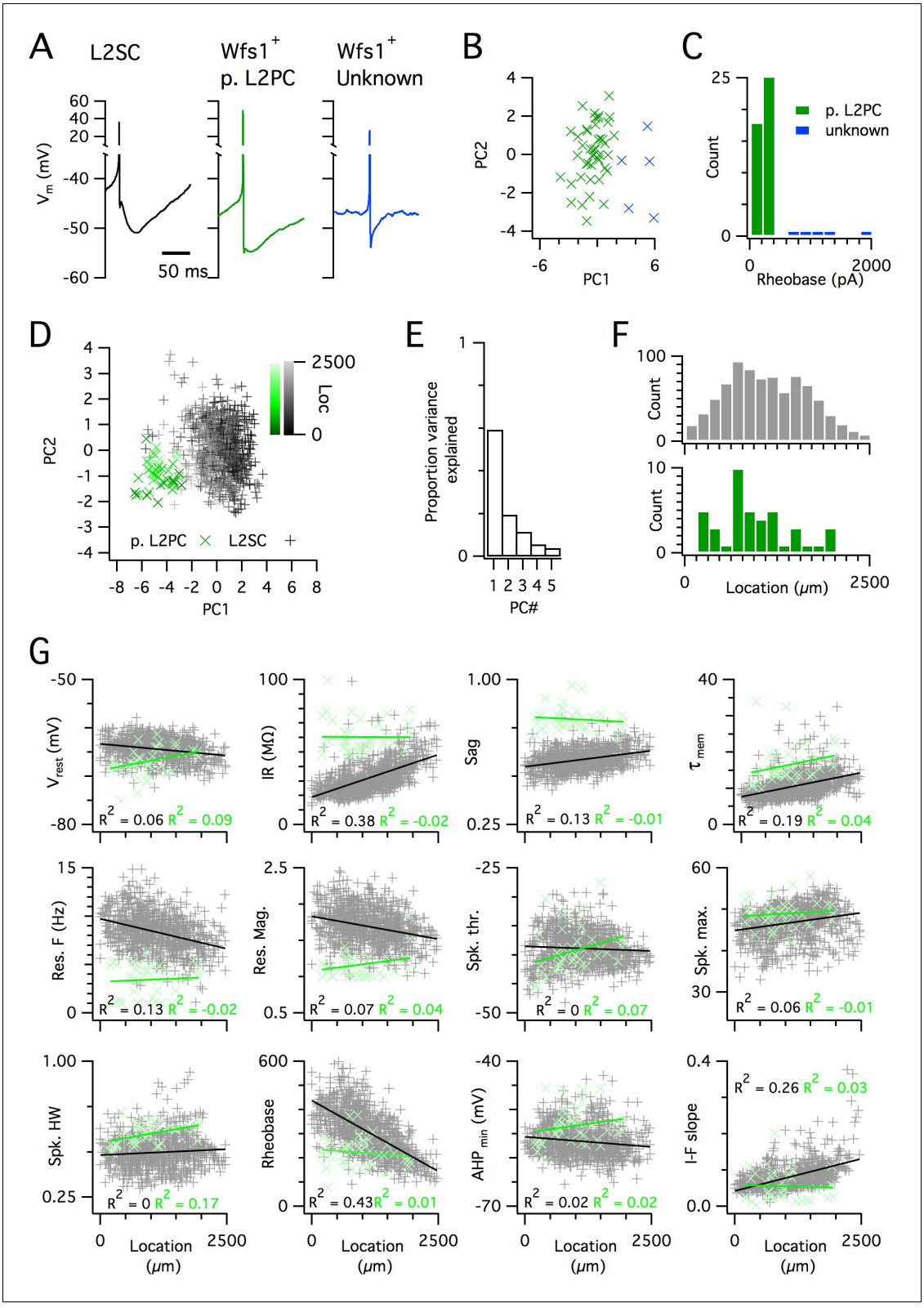

Figure 3. Distinct and dorsoventrally organized properties of layer 2 stellate cells. (**A**) Representative action potential after hyperpolarization waveforms from a SC (left), a pyramidal cell (middle) and an unidentified cell (right). The pyramidal and unidentified cells were both positively labelled in *Wfs1*^{Cre} mice. (**B**) Plot of the first versus the second principal component from PCA of the properties of labelled neurons in *Wfs1*^{Cre} mice reveals two populations of neurons. (**C**) Histogram showing the distribution of rheobase values of cells positively labelled in *Wfs1*^{Cre} mice. The two groups

Figure 3 continued on next page

Figure 3 continued

identified in panel (B) can be distinguished by their rheobase. (**D**) Plot of the first two principal components from PCA of the properties of the L2PC (n = 44, green) and SC populations (n = 836, black). Putative pyramidal cells (x) and SCs (+) are colored according to their dorsoventral location (inset shows the scale). (**E**) Proportion of total variance explained by the first five principal components for the analysis in panel (**D**). (**F**) Histograms of the locations of recorded SCs (upper) and L2PCs (lower). (**G**) All values of measured features from all mice are plotted as a function of the dorsoventral location of the recorded cells. Lines indicate fits of a linear model to the complete datasets for SCs (black) and L2PCs (green). Putative pyramidal cells (x, green) and SCs (+, black). Adjusted R^2 values use the same color scheme.

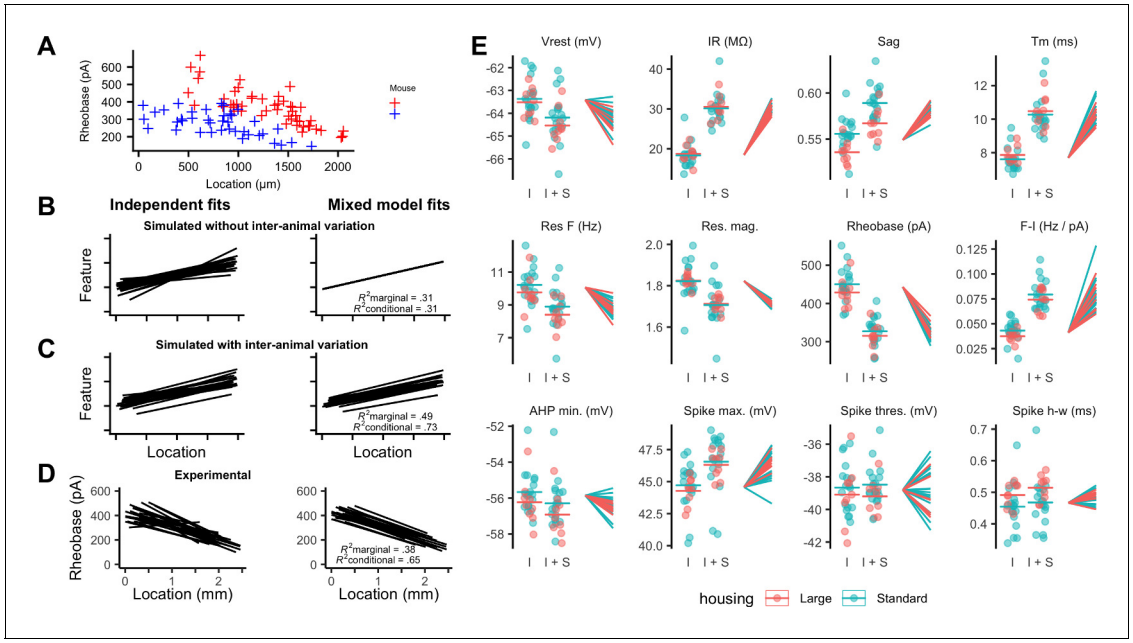

Figure 4. Inter-animal variability and dependence on environment of intrinsic properties of stellate cells. (**A**) Examples of rheobase as a function of dorsoventral position for two mice. (**B, C**) Each line is the fit of simulated data from a different subject for datasets in which there is no inter-subject variability (**B**) or in which intersubject variability is present (**C**). Fitting data from each subject independently with linear regression models suggests intersubject variation in both datasets (left). By contrast, after fitting mixed effect models (right) intersubject variation is no longer suggested for the dataset in which it is absent (**B**) but remains for the dataset in which it is present (**C**). (**D**) Each line is the fit of rheobase as a function of dorsoventral location for a single mouse. The fits were carried out independently for each mouse (left) or using a mixed effect model with mouse identity as a random effect (right). (**E**) The intercept (I), sum of the intercept and slope (I + S), and slopes realigned to a common intercept (right) for each mouse obtained by fitting mixed effect models for each property as a function of dorsoventral position.

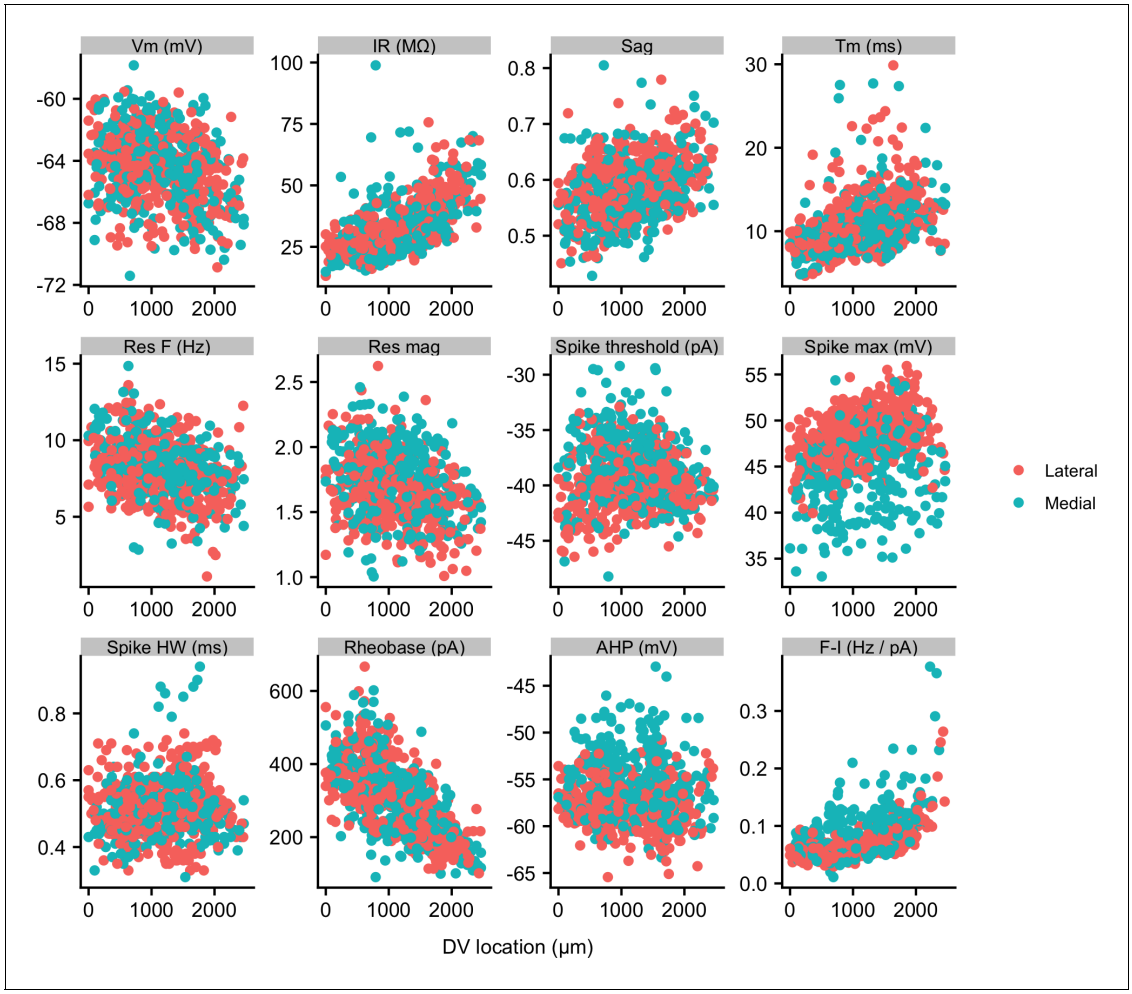

Figure 4—figure supplement 1. Properties of SCs in medial and lateral slices. Membrane properties of SCs from slices containing more medial (blue) and more lateral (red) parts of the MEC plotted as a function of dorsal ventral position. Neurons from more medial slices had a higher spike threshold, a lower spike maximum and a less-negative spike after-hyperpolarization (see ***Supplementary file 6***). Properties are labelled as in ***Figure 2***.

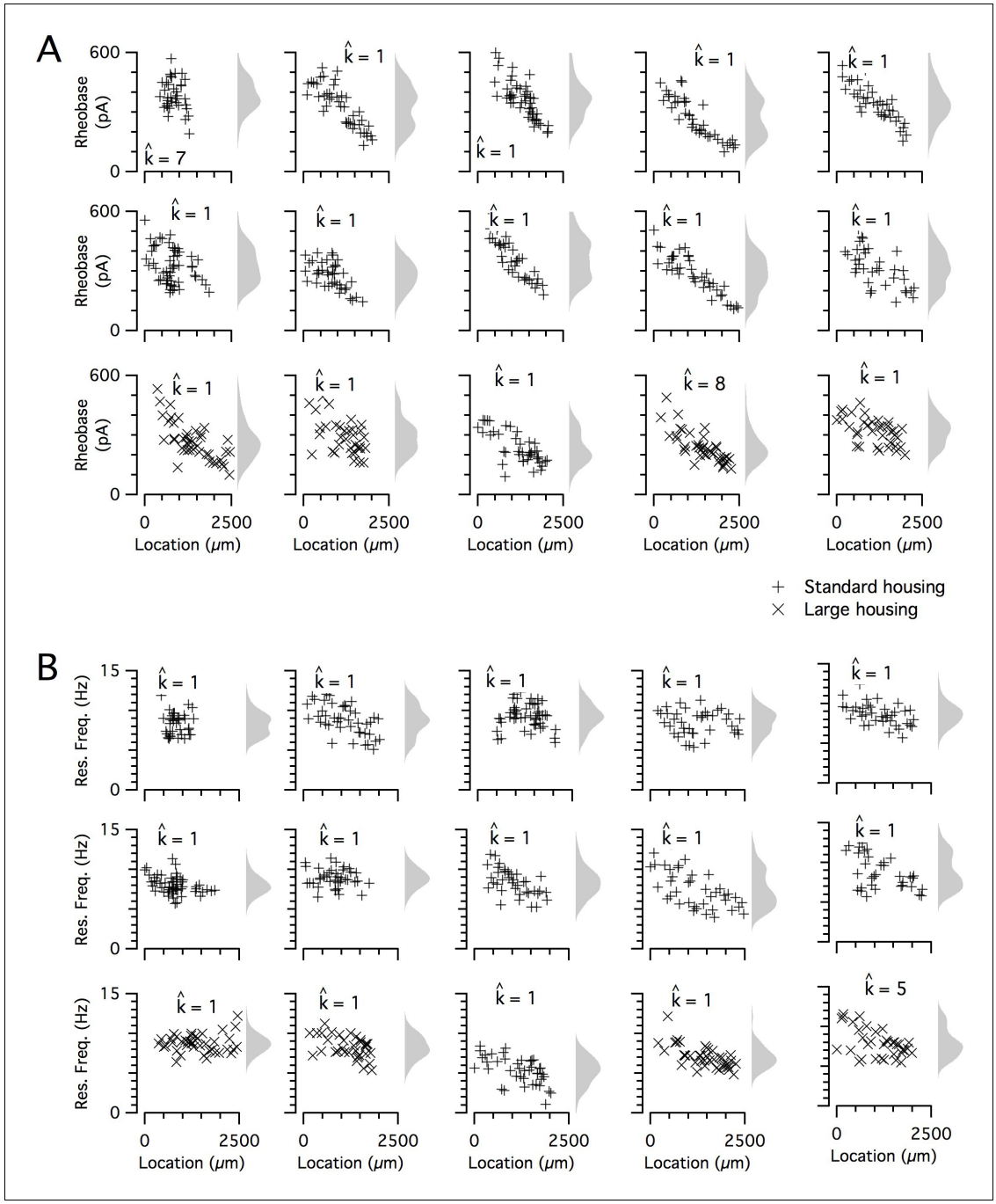

Figure 5. Rheobase and resonant frequency do not have a detectable modular organization. (**A, B**) Rheobase (**A**) and resonant frequency (**B**) are plotted as a function of dorsoventral position separately for each animal. Marker color and type indicate the age and housing conditions of the animal ('+' standard housing, 'x' large housing). KSDs (arbitrary bandwidth, same for all animals) are also shown. The number of clusters in the data (k_{est}) is indicated for each animal ($\hat{k}$).

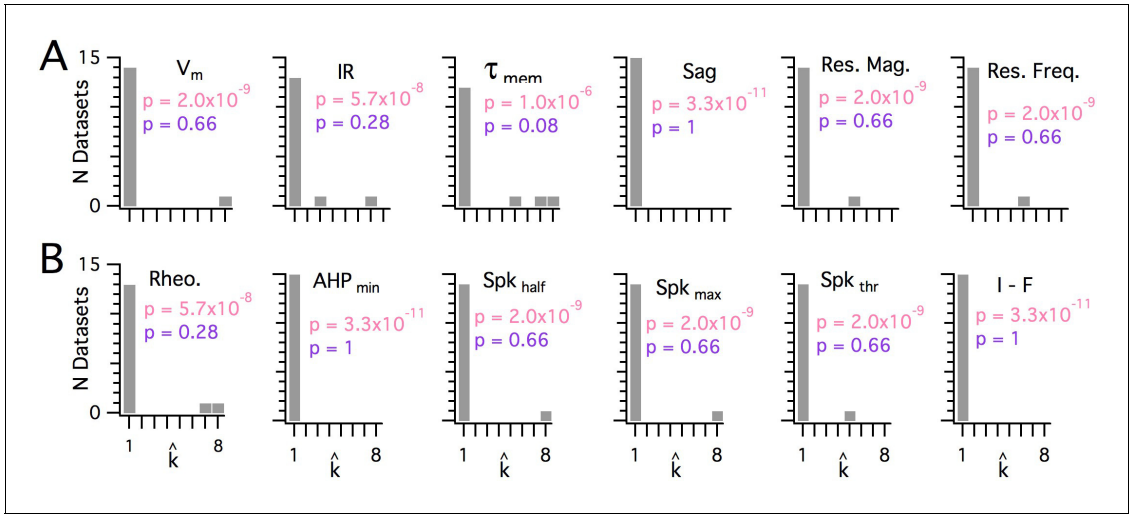

Figure 6. Significant modularity is not detectable for any measured property. (**A, B**) Histograms showing the k_{est} ($\hat{k}$) counts across all mice for each different measured sub-threshold (**A**) and supra-threshold (**B**) intrinsic property. The maximum k evaluated was 8. The proportion of each measured property with $k_{est}>1$ was compared using binomial tests (with N = 15) to the proportion expected if the underlying distribution of that property is always clustered with all separation between modes $\geq$5 standard deviations (pink text), or if the underlying distribution of the property is uniform (purple text). For all measured properties, the values of k_{est} ($\hat{k}$) were indistinguishable ($p>0.05$) from the data generated from a uniform distribution and differed from the data generated from a multi-modal distribution ($p<1\times10^{-6}$).

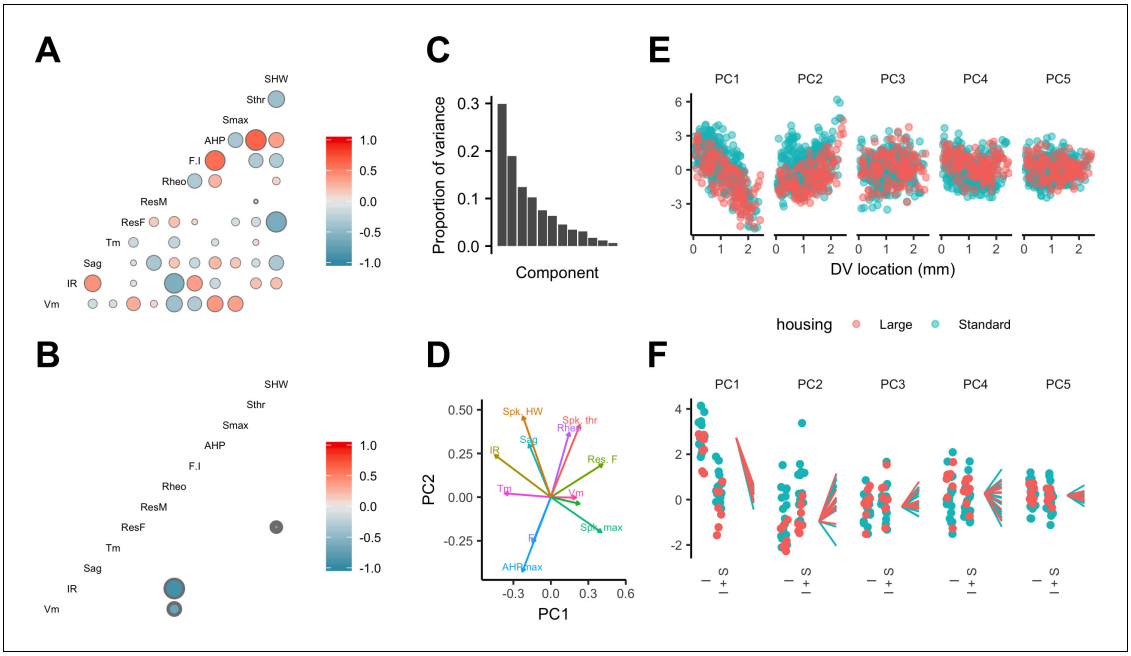

Figure 7. Feature relationships and inter-animal variability after reducing dimensionality of the data. (**A, B**) Partial correlations between the electrophysiological features investigated at the level of individual neurons (**A**) and at the level of animals (**B**). Partial correlations outside of the 95% basic bootstrap confidence intervals are color coded. Non-significant correlations are colored white. Properties shown are the resting membrane potential (Vm), input resistance (IR), membrane potential sag response (sag), membrane time constant (Tm), resonance frequency (Rm), resonance magnitude (Rm), rheobase (Rheo), slope of the current frequency relationship (FI), peak of the action potential after hyperpolarization (AHP), peak of the action potential (Smax) voltage threshold for the action potential (Sthr) and half-width of the action potential (SHW). (**C**) Proportion of variance explained by each principal component. To remove variance caused by animal age and the experimenter identity, the principal component analysis used a reduced dataset obtained by one experimenter and restricted to animals between 32 and 45 days old (N = 25, n = 572). (**D**) Loading plot for the first two principal components. (**E**) The first five principal components plotted as a function of position. (**F**) Intercept (I), intercept plus the slope (I + S) and slopes aligned to the same intercept, for fits for each animal of the first five principal components to a mixed model with location as a fixed effect and animal as a random effect.

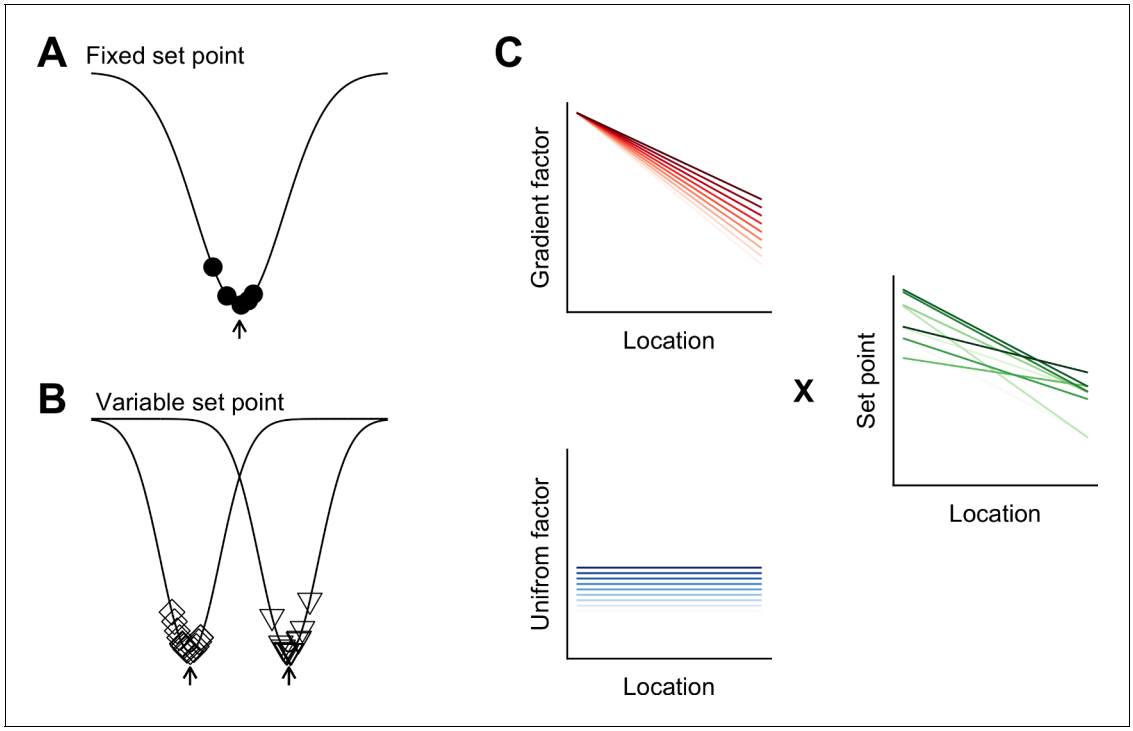

Figure 8. Models for intra- and inter-animal variation. (**A**) The configuration of a cell type can be conceived of as a trough (arrow head) in a developmental landscape (solid line). In this scheme, the trough can be considered as a set point. Differences between cells (filled circles) reflect variation away from the set point. (**B**) Neurons from different animals or located at different dorsoventral positions can be conceptualized as arising from different troughs in the developmental landscape. (**C**) Variation may reflect inter-animal differences in factors that establish gradients (upper left) and in factors that are uniformly distributed (lower left), combining to generate set points that depend on animal identity and location (right). Each line corresponds to schematized properties of a single animal.